

# Pleomorphism in Biological Units of Life: Morphological Heterogeneity in Cells Does Not Translate Uniformly to Subcellular Components

Pragya Singh and Aditya Mittal\*

Cite This: <https://doi.org/10.1021/acsomega.3c10062>

Read Online

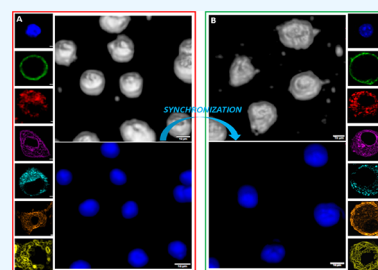
ACCESS |

Metrics &amp; More

Article Recommendations

Supporting Information

**ABSTRACT:** The interplay of the three-dimensional (3D) distribution of various subcellular components and their interactions are expected to control overall cellular morphology in biology. In this study, we aimed to determine whether the pleomorphism observed at the whole-cell level is being reflected by the components constituting the cells by focusing on the 3D distribution of pixel intensities at the single-cell level of the whole (cell) and its parts (the seven subcellular components of the cells—self-assemblies of smaller units). We rigorously acquired and analyzed the image data of RAW264.7 cells at the single-cell level. We report asymmetries in the spatial distribution of pixel intensities at the whole-cell and subcellular component levels along with the occurrence of alterations when pleomorphism is reduced by synchronization of the cell cycle. From our repertoire of seven subcellular components, we report ER, mitochondria, and tubulin to be independent of whole-cell apico-basal heterogeneity of optical density while nuclear, plasma membrane, lysosomal, and actin fluorescence distributions are found to contribute to the apico-basal polarity of the whole cell. While doing so, we have also developed an image analysis algorithm utilizing 2D segmentation to analyze the single cells in 3D using confocal microscopy, a technique that allows us to analyze cellular states in their native hydrated state.



## INTRODUCTION

“In the case of all things which have several parts and in which the totality is not, as it were a mere heap, but the *whole is something besides the parts, ...*,” an Aristotle quote<sup>1</sup> has been inspiring numerous researchers to delve into the areas of the emergent nature of various systems in pursuit of understanding the origin of life to ultimately construct an artificially emergent system.<sup>2</sup> Apart from numerous lipid-based vesicles,<sup>3</sup> nonlipids are also being used to study the emergent behavior of biological systems while attempting to define an application area of such systems.<sup>4–6</sup> We earlier studied the structural characteristics of reversible self-assemblies of bispidine pseudopeptides, the vesicle of which found their use in the cellular uptake of therapeutic molecules.<sup>5</sup> However, it is imperative to study readily accessible naturally emergent systems, cells (*the basic functional units of life*), and their components thoroughly to gain better insights into the emergence of collective structural properties of biological systems, which recent advances in the field have demonstrated.

At a molecular-assembly level, a successful attempt at J. Craig Venter Institute toward the construction of an artificial cell, JCVI syn 3.0, using a minimum of 493 mycoplasma genes as essential survival genes is a big step toward synthetic biological system construction.<sup>7</sup> JCVI syn 3.0 is a culmination of DNA, RNA (including tRNA, mRNA), lipid plasma membrane, ribosomes, membrane-spanning proteins, enzymes involved with DNA (such as topoisomerases and polymerases)

and metabolism, and protein synthesis factors. However, despite having the same genetic makeup, the naturally emergent systems, cells, have been known to depict the heterogeneities at various mechanistic and molecular levels, with the most observable heterogeneity being morphological heterogeneity.<sup>8</sup> In biology, cell morphology is known to be highly characteristic of its tissue and organelles and the constituents of cells are spatially and temporally regulated to be specialized for the shape, symmetry, and function of cells.<sup>8</sup> At any given moment, cells within a population are involved in diverse biochemical processes. In order to attribute the observed morphological heterogeneities at the population level to this diversity in biochemical processes taking place in different cells at a given point in time, it becomes imperative to examine the spatial organization of subcellular components and correlate them with linked biochemical processes. Despite advances in three-dimensional cellular architecture analysis using sophisticated imaging techniques, our study focuses on leveraging 3D spatial information to explore how phenotypic plasticity at the subcellular level contributes to the observed

**Received:** December 16, 2023**Revised:** April 13, 2024**Accepted:** May 14, 2024

whole-cell morphological heterogeneity in populations using a technique that is commonly used as a 2D tool to enhance the signal:noise ratio in fluorescence images.<sup>9</sup> A variety of methods can be used to study the cellular architecture at the whole-cell level and at the subcellular component level, with image-based analyses largely dominating the field with various microscopy techniques, such as light microscopy (shapes and sizes of cells), confocal microscopy (three-dimensional morphology of cells), and electron microscopy (ultrastructure of cells), data from which can be used to quantify various morphological features.<sup>10,11</sup>

In this study, we explore the nature of three-dimensional spatial morphological pleomorphism at a single-cell level and whether the pleomorphism observed at the whole-cell level is being reflected by or translated into the pleomorphism at the level of subcellular compartments. In other words, whether the whole is indeed something other than its parts. Morphological heterogeneity in any cell population across random time points is dynamic and time-dependent, driven by diverse biochemical processes. Therefore, we set up a control condition when the dynamics of morphological changes are minimized, which we achieve by synchronizing the cell cycle at the G2/M phase to validate our findings while demonstrating that observed morphological diversities (result of averaging the observations made in an asynchronous population) already encompass variations expected across different phases, reinforcing the robustness of our initial observations. To this end, we employed murine macrophage-like cells, RAW264.7 cells. These cells have two distinct well-established morphologies: irregular, spindle-shaped and rounded, spherical-shaped; hence, the population was categorized into asymmetric and symmetric subsets to study pleomorphy within the two subsets. The study aims to utilize the cellular image data to quantify the differences between 3D geometric sections using pixel intensities for the whole cell as well as for various subcellular components in their native hydrated states using well-established organelle-specific fluorescent chemical agents through confocal microscopy.

## ■ EXPERIMENTAL SECTION

**Cell Culture and Synchronization.** RAW264.7 cells were cultured in T25 Nest cell culture flasks in complete media comprising Dulbecco's modified Eagle's medium (Gibco, Cat. No.: 12430-054), 5% fetal bovine serum (Gibco, Cat. No.: 10270106), and 1% penicillin–streptomycin (5000 U/mL) (Gibco, Cat. No.: 15070063) in 5% CO<sub>2</sub> at 37 °C. The cells were passed using 0.25% trypsin (Gibco, Cat. No.: 25200072). At passage 4, the cells were counted on a hemocytometer after trypsinization and 2 mL of suspension (~50,000 cells + complete media) was placed in a coverslip-containing 35 mm petri dish. Cells were allowed to attach to the coverslip and grow at 37 °C in 5% CO<sub>2</sub> for 12 h. For cell cycle synchronization, thymidine (Sigma-Aldrich, Cat. No.: T1895) containing complete media (with the final thymidine concentration at 2 mM) was added in the petri dish and cells were incubated for 20 h. After 20 h, thymidine-containing media were removed and cells were washed twice with 1× PBS. The cells were allowed to grow in complete media for 5 h. After 5 h, the cells were incubated in complete media containing 50 ng/mL nocodazole (Sigma-Aldrich, Cat. No.: M1404) for 11 h. After 11 h, the nocodazole-containing media were removed and the cells were washed three times with 1× PBS.<sup>12</sup>

**Organelle-Specific Fluorescence Staining.** The staining of the seven subcellular assembly components, nucleus, cell membrane, mitochondria, endoplasmic reticulum, lysosome, actin, and tubulin, was carried out using well-established organelle-specific fluorescent dyes. The staining protocols of the organelles were optimized. Cells were stained with Hoechst 33342 (Thermo Fisher Scientific, Cat. No.: H21492) (15 μg/mL) for 15 min at room temperature in 1× PBS to stain nucleus. For the plasma membrane, cells were stained with wheat germ agglutinin fluorescein conjugate (Thermo Fisher Scientific, Cat. No.: W834) (5 μg/mL) for 30 min at room temperature in 1× HBSS. For mitochondrial staining, cells were stained using MitoTracker Orange CMTMRos (Thermo Fisher Scientific, Cat. No.: M7510) (50 nM) for 10 min in serum-free DMEM at room temperature. For staining endoplasmic reticulum, cells were kept in 1× HBSS solution containing ER-Tracker Blue/White DPX (Thermo Fisher Scientific, Cat. No.: E12353) (100 nM) for 30 min at 37 °C. Cells were stained using LysoTracker Deep Red (Thermo Fisher Scientific, Cat. No.: L12492) (1 μM) in 1× PBS for 30 min at 37 °C to label lysosomes. For labeling actin, cells were stained using BODIPY Phalloidin (Thermo Fisher Scientific, Cat. No.: B3475) (30 U) for 30 min in 1× PBS after fixation with PBS containing 2% paraformaldehyde (Sigma-Aldrich, Cat. No.: TCL119) and 0.05% glutaraldehyde solution (Sigma-Aldrich, Cat. No.: 340855) and permeabilization with 0.1% Triton X-100 (Sigma-Aldrich, Cat. No.: X100) for 3 min at room temperature. Cells were stained using Paclitaxel Oregon Green 488 (Thermo Fisher Scientific, Cat. No.: P22310) (1 μM) for 90 min in serum-free media at 37 °C to fluorescently label tubulin. A detailed experiment protocol is shown in Figure S2.

**Confocal Microscopy and Image Acquisition.** After staining, the samples were washed three times with the corresponding staining medium without the fluorescent stain and then kept in serum-free media. The slides were prepared for imaging using serum-free medium as the mountant. The imaging of the samples was done in an FV1200 Olympus Confocal microscope in LUCPLFLN 60× objective, and images were captured using a Photometrics Evolve Delta camera. The fluorescence was obtained using 405, 473, and 548 nm laser at 30, 44, and 48% transmissivity, respectively, and 2 μs/Pixel frame rate. Unstained cells were used as a negative control to set imaging parameters. Different fields representing different microenvironmental areas were captured. The image data was exported in .tif format for further image processing and analysis.

**Image Analysis and Quantification.** The image data analyzed are a culmination of data gathered on different days to represent different random time points in the cell cycle as well as from various duplicate sets of RAW264.7 cells to include as many heterogeneous cells as possible. The images were imported in MATLAB 2021a, and the middle image of the *z*-section was used to define the ROI manually based on the assumption that the best-focused image in the *z*-section will be the center image. If *N* is the number of DIC images in a *z*-section, then the  $N/2^{\text{th}}$  image is the middle image if *N* is even and the  $(N + 1)/2^{\text{th}}$  image when *N* is odd. ROI was defined around the cell boundary manually, the ROI array was saved at the image folder location, and the centroid and circularity values of each cell were retrieved and saved in Excel for further segregation into asymmetric and symmetric shapes. Pixel coordinates and corresponding pixel values of each ROI were

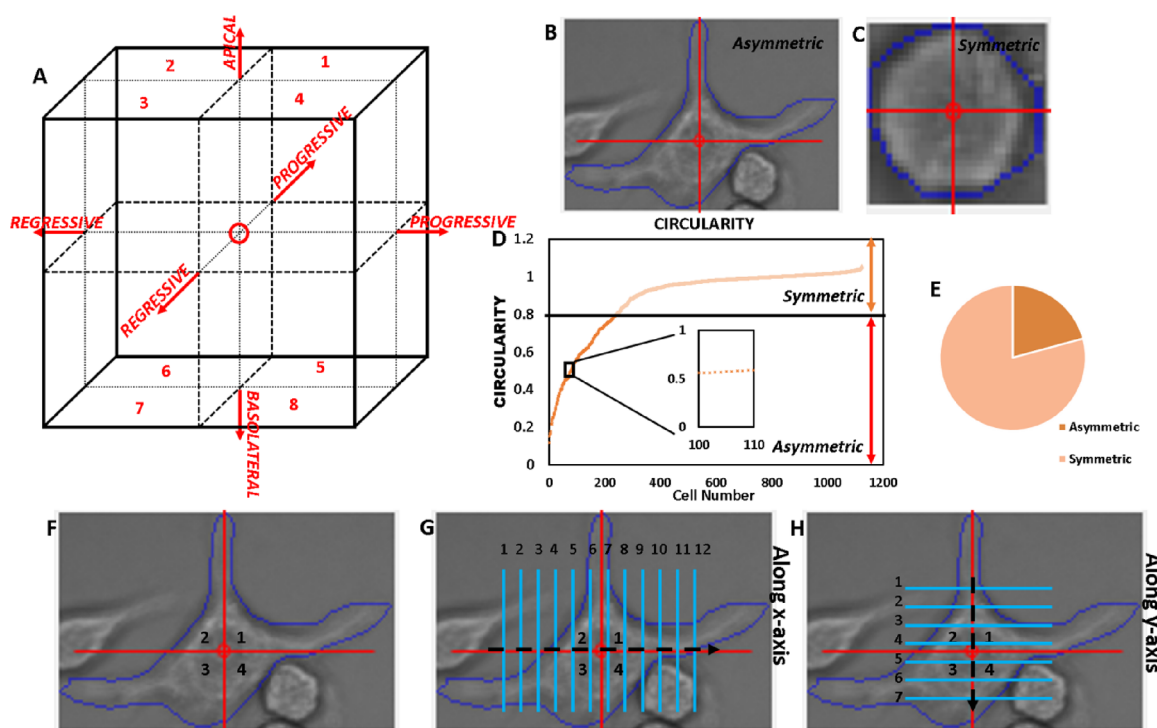


**Figure 1.** (A) Division of 3D space into octants around the centroid (marked in red) and the sides associated with octants along the three axes. (B, C) Representative asymmetrical and symmetrical cells, respectively, with overlaying ROI (blue boundary) of asynchronous RAW264.7 cell population. (D) Dot plot of the circularity value and the threshold for classifying the cells into asymmetrical and symmetrical subsets. The inset shows that the circularity values are discrete and not continuous. (E) Percentage of asynchronous asymmetrical (dark orange, ~21%) and symmetrical (light orange, ~79%) RAW264.7 cell population ( $N = 1124$ ). (F) Top view of the asymmetric cell divided into quadrants around the centroid (red "+"). (G, H) Frame reading pattern along the  $x$ - and  $y$ -axes.

further used for the image analysis. The segregation of pixel coordinates was done in all three directions with a  $0.1 \mu\text{m}$  step size between XY planes along the  $z$ -axis and a  $0.4 \mu\text{m}$  distance between YZ and XZ planes along the  $x$ - and  $y$ -axes, respectively, and into the eight octants around the centroid of a single-cell  $z$ -stack. An average pixel value of each octant for each cell is calculated and saved in MS Excel for further analysis. A detailed image data processing flowchart is shown in Figure S1. A MATLAB code has been provided as a Supporting Information file titled "Image\_Processing\_code" in .pdf format. Normalization of the data (APV) was carried out for each field to remove any technical variations, such as transmissivity power of the laser, PMT (photomultiplier tube) voltage, gain, offset, and other parameters, including handling errors during the staining process.<sup>13</sup> The highest APV from the octant data for a field was equated to one, and the other values were calculated accordingly.

Having used well-established organelle-specific fluorescent labels as the reporters of three-dimensional distribution of organelle-specific fluorescence and assuming they uniformly stain the organelles in different cells, we further evaluated the total pixel value for each cell in a field to check for uniform staining and further the average pixel value for each octant for each cell to check if the fluorescence intensities are uniformly distributed in the 3D space of the cell. Based on the initial result, the distribution of APVs along the three axes was plotted after segregating the 3D space into apical (octants 1–4) and basal (octants 5–8) sections, progressive (octants 1, 2, 5, 6) and regressive (octants 3, 4, 7, 8) sections along the  $y$  axis, and progressive (octants 2, 3, 6, 7) and regressive (octants 1, 4, 5, 8) sections along the  $x$ -axis (Figure 1A) to analyze the

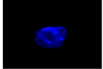
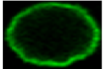
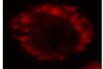
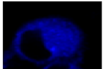
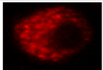
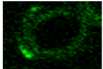
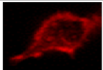

organelle distribution variability in a cell population. The population distribution for APVs in each octant was plotted after frequency normalization to determine the APV distribution uniformity in a population in asynchronous and synchronized conditions.

Setting the circularity value filter at 0.8, the cells were further segregated into symmetrical cells (for values greater than or equal to 0.8) and asymmetrical cells (for values less than 0.8). A threshold of 0.8 was chosen based on a 1971 study stating a value of 0.79 to be a regular square and 0.61 to be triangular.<sup>14</sup> The cells with values 0.8 and above have been categorized as circular in shape, which led us to set the threshold at 0.8 to consider the cell as circular and therefore symmetrical and the value was further confirmed by visually examining the whole-cell images.<sup>14</sup>

The quantification of cell neighbors was carried out by labeling individual cells as either asymmetrical or symmetrical based on circularity index using the image processing algorithm and counting the number of cells (along with subset category) with a particular number and type of neighbor. The cells that have their cell boundaries (defined by region of interest) touching are classified as neighbors of each other.

**Statistical Analysis.** Data are shown in mean  $\pm$  SE. The processed data were subjected to a two-tailed unpaired Student's  $t$  test to derive the significance of the differences seen in the data set in Microsoft Excel. A  $p$ -value of less than 0.05 was considered significant.  $t$ -test was applied between APVs of different sections to check for significant differences between intensity signals of different sections as well as between asymmetrical and symmetrical cell data sets along with asynchronous and synchronous data sets. Depending upon a

**Table 1.** List of Fluorophores, the Respective Organelle Stained, the Mechanism of Staining, and a Representative Captured Image

Fluorophore	Component Imaged	Mechanism of Staining	Representative Image
Hoechst	Nucleus	Hoechst binds into the minor groove of DNA and exhibits distinct fluorescence emission spectra that are dependent on dye:base pair ratios	
WGA-Fluorescein conjugate	Cell Membrane	Wheat germ agglutinin selectively binds to N-acetylglucosamine and N-acetylneuraminic acid (sialic acid) residues	
MitoTracker CMTMRos	Mitochondria	Passively diffuse across the plasma membrane and accumulate in active mitochondria	
ERTracker Blue-White DPX	Endoplasmic Reticulum	Selectively labels Endoplasmic Reticulum membrane	
LysoTracker	Lysosome	Fluorophore linked to a weak base and selectively stain acidic organelles.	
Paclitaxel Oregon Green	Tubulin	Fluorophore is attached to the 7-carbon of the paclitaxel that permits selective binding of the probe to microtubules.	
BODIPY Phalloidin	Actin	Phalloidin binds F-actin with high selectivity and fluorophore provides bright red color	
Not Applicable	Whole cell	Not Applicable	

significant *p*-value, the difference between the vertical apical and basolateral sections and lateral regressive and progressive sections was considered as significant, and the existence of heterogeneity in signal distribution was concluded. Insignificant *p*-values led us to conclude the absence of any considerable differences between sections and hence the polarity of the signal distribution.

## RESULTS

Well-established fluorophores known to specifically label subcellular components were used to fluorescently label the seven subcellular components in RAW264.7 cells. Table 1 lists the commercially available fluorophore names, the components they label, the mechanism of labeling, and a representative image of the fluorophore labeled specific component of RAW264.7 cells.

The DIC (differential interference contrast) images, captured alongside organellar fluorescent images, were used to define each cell's ROI (region of interest) based on the outline visible to the naked eye for the asynchronous and synchronized RAW264.7 population, and all the further image processing and analysis were confined to the ROI of each cell. A total of 1124 asynchronous and 563 synchronized cells have been imaged with the organelle-specific number mentioned in Table 2. The 3D space of the cells was divided into the eight octants around the centroid of the cell's *z*-stack, as shown in Figure 1A. The cells in the populations were categorically subdivided into asymmetric and symmetric cell categories for further analysis based on a cutoff criterion. Figure 1B,C shows representative asymmetrical and symmetrical cells. The circularity value of the midsection image cell was derived. The cells with values equal to or greater than 0.8 were categorized as symmetric, while the cells with values less than 0.8 were categorized as asymmetric (Figure 1D). Notably, the number of asymmetric cells is less than the number of symmetric cells, with asymmetric cells comprising 21% of the

**Table 2.** Number of Cells Imaged for Each Organelle in Asynchronous and Synchronized RAW264.7 Cell Populations<sup>a</sup>

S. no.	organelle	asymmetric cells	symmetric cells	total
Asynchronous				
1.	nucleus	35 (13%)	228 (87%)	263
2.	plasma membrane	28 (24%)	91 (76%)	119
3.	mitochondria	44 (17%)	213 (83%)	257
4.	ER	39 (32%)	83 (68%)	122
5.	lysosome	36 (27%)	98 (73%)	134
6.	actin	53 (32%)	113 (68%)	166
7.	tubulin	13 (6%)	187 (94%)	200
Synchronized				
1.	nucleus	23 (18%)	103 (82%)	126
2.	plasma membrane	9 (11%)	73 (89%)	82
3.	mitochondria	3 (2%)	150 (98%)	153
4.	ER	3 (2%)	150 (98%)	153
5.	lysosome	9 (11%)	73 (89%)	82
6.	actin	13 (12%)	94 (88%)	107
7.	tubulin	3 (3%)	107 (97%)	110

<sup>a</sup>The cells were stained for multiple organelles at a time. Hence, some of the numbers are repeated twice.

population (240 out of 1124) while symmetric cells make up 79% of the population. However, the number of pixels occupied by asymmetric cells is larger (Figure 1E).

The "average pixels" of each plane in the Cartesian coordinate system's three directions and the APVs of each octant (defined around the centroid of the cell) were calculated (values in Supplementary Excel Files). The segregation of the pixels into quadrants and subsequent octants is shown in Figure 1F, along with the frame reading pattern along the *x*- and *y*-axes in Figure 1G and H, respectively. We analyzed raw, unprocessed images to minimize human interference that might affect data inter-

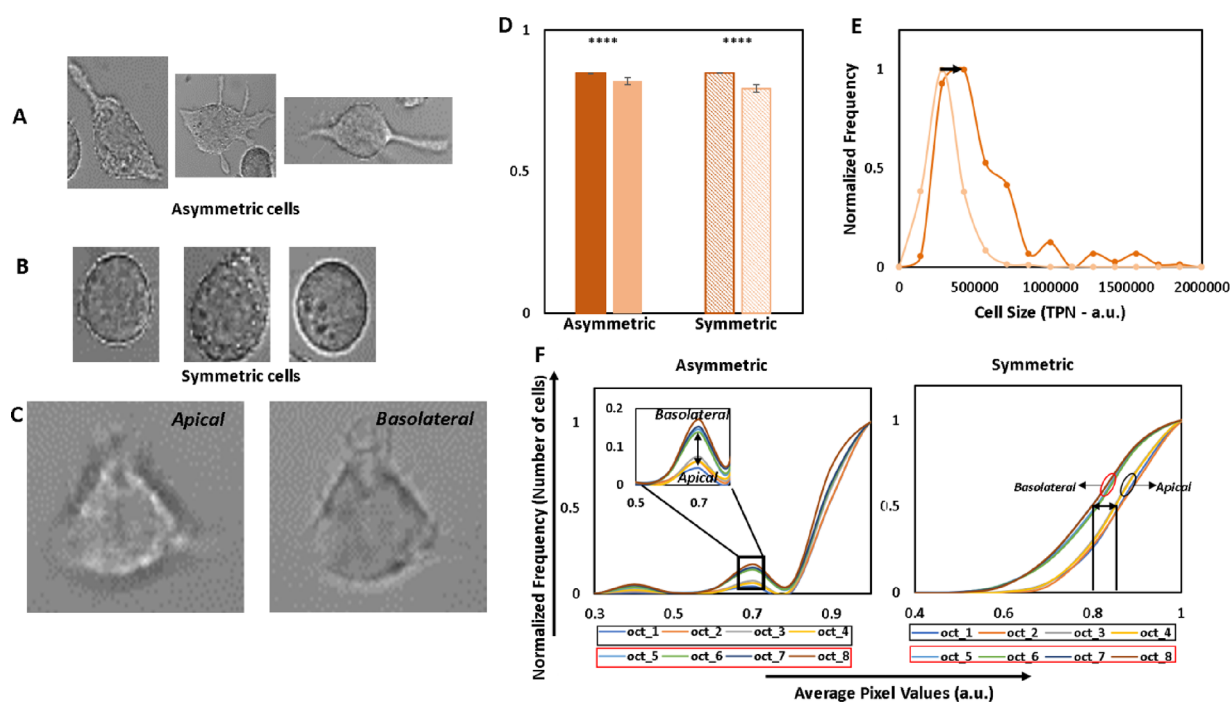


**Figure 2.** Three representative asymmetrical (A) and symmetrical (B) RAW264.7 cells in an asynchronous population. (C) Representative apical and basolateral sections of a single cell showing different optical intensities in the sections. (D) APV distribution bars in  $z$ -sections along the  $z$ -axis in the DIC images of the asynchronous RAW264.7 cell population (mean  $\pm$  SE). Solid bars represent an asymmetric subset of cells, and patterned bars represent a symmetric cell subset. The apical sections are depicted by dark-orange bars, and the basolateral areas are depicted by light-orange bars. The level of significance is shown by \*. (E) Normalized frequency distribution of the total pixel number of the asynchronous RAW264.7 cells [asymmetric cells—dark orange, symmetric cells—light orange]. (F) Normalized cumulative frequency distribution of the number of cells for DIC images at different APVs in each octant for the asynchronous RAW264.7 cell population.

pretation. Hence, all of the calculations were done on raw data, including pixel intensities in DIC images. During analysis, the data for each field were normalized to minimize the technical variations occurring during the image acquisition process. For this, the highest average pixel value was equated to 1 and the rest were derived relatively.

**The Pleomorphic Nature of the Cell Population.** The DIC images of the cells were visualized to assess the differences visible to the naked eye. We observed differences in the shapes of the cells (Figure 2A and B). Some cells had a rounder shape categorized as symmetric, while others appeared to be spread out with no representative shape, which we refer to as asymmetric. Even within the subcategories, the differences in the optical densities of different parts of the cells were observable within the same section of the same  $z$ -stack (Figure 2A,B). The circularity plot shows that none of the circularity values were overlapping and were indeed discrete rather than continuous (Figure 1D). The number of unique circularity values was equal to the number of cells. Upon visual examination, we can also observe the variation in the pixel intensities in the  $z$ -stack from the apical (brighter) to the basolateral (darker) section (Figure 2C).

**Impact of Neighborhood on Cellular Morphology.** The fields were carefully analyzed to study the impact of the nature of the surrounding cells on cellular morphology. Figure S3 shows the asymmetric and symmetric cells surrounding environments with respect to the surrounding cells' morphological subset, respectively, and the numbers pertaining to that subset are shown in the insets. While the probability of either morphological subset to be surrounded by a symmetric cell is considerably higher than either having an asymmetric subset or

no neighbor at all, the probability of a symmetric cell to be surrounded by a symmetric cell is highest at 0.74. Analysis of the number of neighbors of either morphological subset sharing a boundary with an asymmetric or symmetric cell showed that most of the cells shared their boundaries with only one cell of either morphological subset (insets in Figure S3); that is, if sharing a boundary, most cells would exist in duo rather than clusters, which can be attributed to the cell type rather than a generalized statement applicable to majority of cell types. A maximum of five symmetric and three asymmetric neighbors can surround a cell of either morphological subset.

**Quantitative Image Analysis of 3D Geometric Space of Cells.** After visual examination, we aimed to define the differences observed quantitatively. For this, we studied the pixel intensity distribution along the three axes:  $z$ ,  $y$ , and  $x$ . The average pixel values were plotted for asymmetrical and symmetrical cells for the apical and basolateral sections of the  $z$ -stack and regressive and progressive sections along the  $x$ - and  $y$ -axes (Figure 2D and Figure S6 I-A and II-A). The raw APVs for DIC image  $z$ -stacks captured in correspondence to fluorescent image  $z$ -stacks are listed in Table S6. In DIC images, the pixels in the denser area of the image will have values lesser than the pixels from a nondense area. As expected, the cells' basolateral adherent side was denser in both the asymmetric and symmetric cells. The percentage differences between the apical and basolateral sides of the two subsets were approximately 3 and 6% in asymmetric and symmetric cells, respectively. The normalized cumulative frequency distribution of the octants in both the asymmetric and symmetric cell subsets showed a varying trend in the two subsets (Figure 2F). For asymmetric cells, the difference

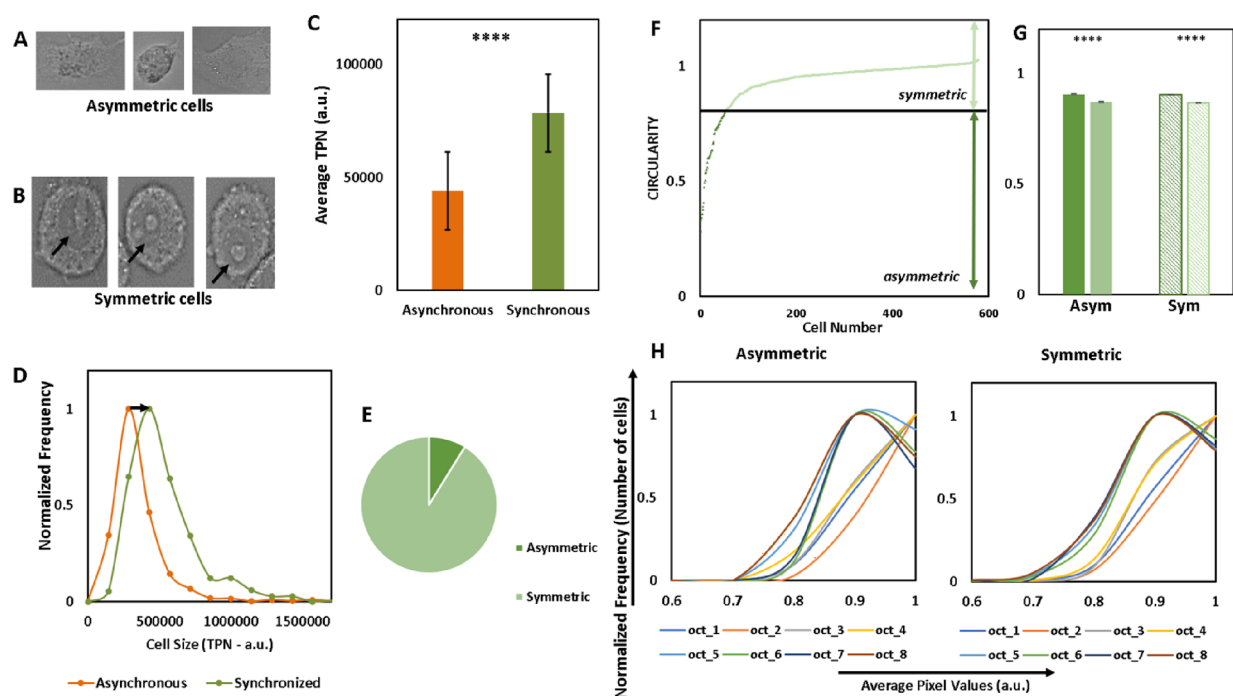


**Figure 3.** (A, B) Three representative asymmetric and symmetric RAW264.7 cells in the synchronized population. (C) Bar graphs showing the average total pixel number of the RAW264.7 cells in the asynchronous (orange) and synchronized (green) populations (mean  $\pm$  SE). (D) Normalized frequency distribution of the total pixel number of the asynchronous (orange) and synchronized (green) RAW264.7 cells. (E) Percentage of asymmetric (dark green,  $\sim$ 9%) and symmetric (light green,  $\sim$ 91%) cells in the synchronized RAW264.7 cell population ( $N = 578$ ). (F) Dot plot of the circularity value and the threshold for classifying the cells into asymmetrical and symmetrical subsets. (G) APV distribution bars in  $z$ -sections along the  $z$ -axis in the DIC images of the synchronized RAW264.7 cell population (mean  $\pm$  SE). Solid bars represent an asymmetric subset of cells, and patterned bars represent a symmetric cell subset. The apical sections are depicted by dark-green bars, and the basolateral areas are depicted by light-green bars. The level of significance is shown by “\*”. (H) Normalized cumulative frequency distribution of the number of cells for DIC images at different APVs in each octant for the synchronized RAW264.7 cell population.

between the basolateral octants 5–8 showed a marked frequency difference at a single APV of 0.7, while in the case of the symmetric cell subset, the frequency distribution between the apical and basolateral octants was consistent throughout. Visual examination showed the asymmetric cells to be more spread out and hence to be in possession of more surface area. This was quantitatively verified by a normalized frequency distribution of the total pixel number occupied by each cell in the  $z$ -stacks, which showed a right shift from the symmetric cell subset (Figure 2E).

**Effects of Cell Cycle Synchronization.** We synchronized the population of the cells to the G2/M phase using the thymidine/nocodazole treatment. The treatment leads to 85% of the population being synchronized at the G2/M phase, which gradually drops after nocodazole release.<sup>12</sup> Therefore, the imaging was done within 4 h after the nocodazole release. Two of the many morphological changes that occur as the cells are about to enter the M phase of the cell cycle are that the cells reportedly attain a rounded morphology and become bigger in size.<sup>15</sup> The image-based analysis performed to check for these two changes confirms the synchronization of the cell population at the G2/M phase using a thymidine/nocodazole treatment. Change in cell shape, along with the change in cell size, were considered indicators of the successful synchronization of the population at the G2/M phase. We observed that the percentage of the asymmetric cell reduces to 9% from 21% upon synchronization while the cell size increases by 78%, the indicator for which is the total number of pixels (TPN) in the  $z$ -stack of each cell (Figure 3C,E). The frequency distribution

curve of the TPN values shows the shift in the frequency toward the right upon cell cycle synchronization of the population (Figure 3D). While the average APV plots of the apical and basolateral sections of the asymmetric and symmetric cells (both 3% denser on the basolateral side) showed no difference from the trend observed in the asynchronous population, the cumulative frequency distribution of the APV values of the octants for the asymmetric and symmetric subsets of the synchronized population was observed to possess the same trend, but the trend had altered from the trends observed in asynchronous population (Figure 3G,H). The raw APV values for the same are given in Table S8.

Visual examination of the synchronized cells showed that the asymmetric cells were devoid of protrusions, as seen in the asynchronous population (Figure 3A). The symmetric cells were also found to possess a denser round structure within the cells, which was absent in the asynchronous population (Figure 3B). Based on the DIC-based observations at 60 $\times$  at the whole-cell level, we can say that “no two cells are identical”. The variations in the percentage of cells in each shape subset and the cell size were the two parameters observed, which themselves were liable to change upon a change in the cell cycle.

Analyzing the type and number of neighbors of an asymmetric or symmetric cells shows an increase in the probability of a cell being surrounded by a symmetric cell while the probability of a cell having only one neighbor is still the highest (Figure S3C,D) while the maximum number of

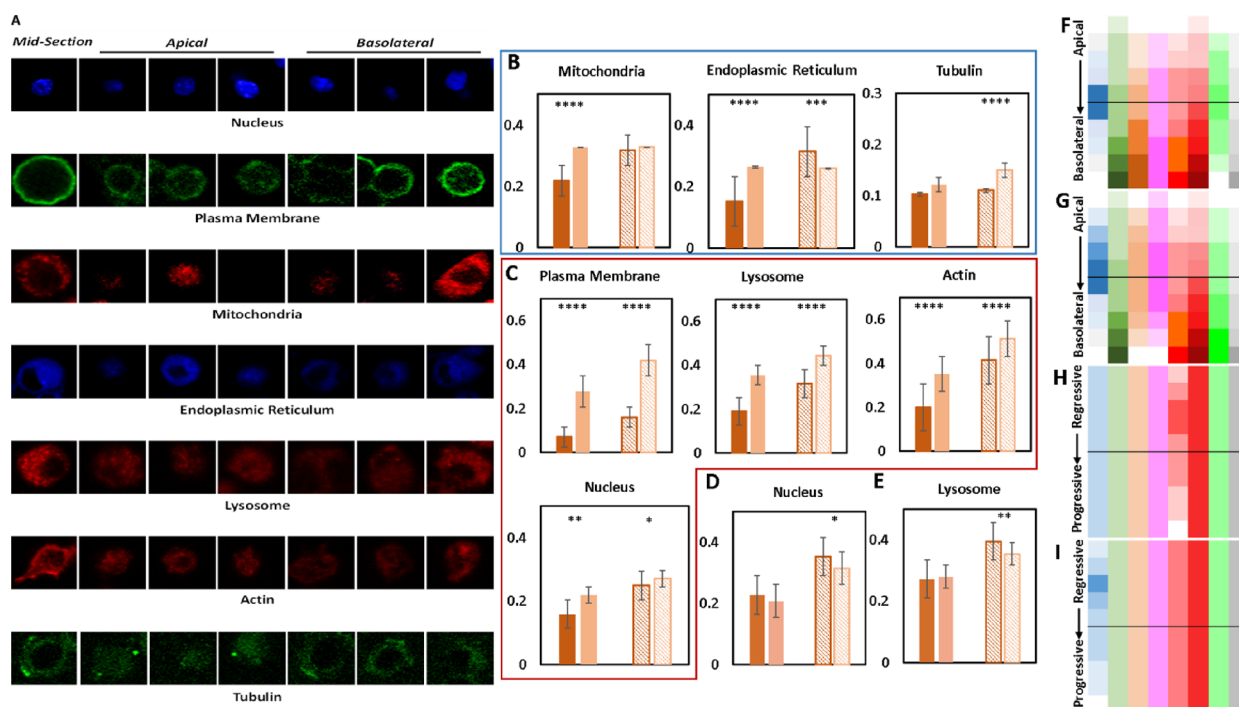


**Figure 4.** (A)  $7 \times 7$  panel of fluorescent images of different organelles in a single cell both in the asynchronous RAW264.7 population. The first image of each panel is a midsection image of a single-cell organelle fluorescence from a z-stack, followed by representative images of one of the apical sections of a z-stack of three single cells, followed by their corresponding basolateral section images. APV distribution bars (B, C) in z-sections along the z-axis and (D, E) laterally along the  $y$ - and  $x$ -axes, respectively, in the asynchronous RAW264.7 cell population (mean  $\pm$  SE). Solid bars represent an asymmetric subset of cells, and patterned bars represent a symmetric cell subset. The apical (B, C) and regressive (D, E) sections are depicted by dark-orange bars, and basolateral (B, C) and progressive (D, E) areas are depicted by light-orange bars. The level of significance is shown by “\*”. The absence of “\*” is considered a lack of polarity. (B) (Blue) Cell-shape-dependent variations in polarity in mitochondria ( $n = 257$ ), endoplasmic reticulum ( $n = 122$ ), and tubulin ( $n = 200$ ) fluorescence. (C) (Red) Polarity independent of cell shape in the nucleus ( $n = 263$ ), plasma membrane ( $n = 119$ ), lysosome ( $n = 134$ ), and actin ( $n = 166$ ) fluorescence. (D) Polarity in nuclear fluorescence along the  $x$ -axis. (E) Polarity in lysosomal fluorescence along the  $y$ -axis. (F–I) Representative diagrams of fluorescence distribution of the organelles along the z-axis (F, G), from apical to basolateral surfaces, and the  $y$ - and  $x$ -axes (H, I), from regressive to progressive surface, respectively, in asymmetric (F) and symmetric (G–I) cell subsets, respectively. The organelles, from left to right, are the nucleus (blue), plasma membrane (dull green), mitochondria (orange), endoplasmic reticulum (pink), lysosome (light red), actin (bright red), tubulin (bright green), and DIC image intensities (gray).

neighbors a symmetric cell can have is 5 and an asymmetric cell has a maximum of 4 neighbors.

**Pleomorphy at the Subcellular Level.** Moving forward to the subcellular level, since we cannot observe the subcellular compartments in DIC images, we fluorescently labeled subcellular components with commercially available and scientifically reported organelle-specific fluorophores to visualize the distribution of different subcellular compartments within the cells to determine the degree of variations in their three-dimensional placement within the cells of a population. The most obvious variation we observed by visual examination of the fluorescent images was the vertical variation in the fluorescence signals (Figure 4A). Few organelle fluorescence signals (nuclear and lysosomal) also showed differential lateral polarity.

To quantify these observations, pixel intensity analysis was carried along the three directions of the Cartesian coordinate system. Preliminary analysis of pixel intensities carried out for nuclear fluorescence highlights the significance of utilizing the APV values to study the 3D distribution of organelles. Figure S4 shows that while the pixel values for nuclear fluorescence in the nine cells were similar, their 3D distribution in the eight octants varied for all nine cells, leading us to proceed further with plotting the APVs for different sections of the cell. The

raw APV values for fluorescently labeled organelles in the asynchronous RAW264.7 cell population are mentioned in Table S5. The fluorescence intensity distributions of seven subcellular compartments, namely, the nucleus, plasma membrane, mitochondria, endoplasmic reticulum, lysosome, actin, and tubulin, were studied. Our primary objective was to determine the number of directions in which the polarity in fluorescence distribution exists. While for most of the organelles, polarity existed along the z-axis, planar polarity was observed in the case of nuclear (8.7% greater regressive fluorescence than progressive fluorescence intensity distributions along the  $x$ -axis, Figure 4D) and lysosomal (11.5% more regressive section fluorescence than progressive fluorescence intensity distributions along the  $y$ -axis, Figure 4E) pixel intensity distributions, which were also shape-dependent with the geometrical polarities existing only in the symmetric cells. The nuclear, plasma membrane, lysosome, and actin fluorescence intensity distributions were independent of the cell shape, with the average pixel intensities being higher on the basolateral side than on the apical side (Figure 4C) resembling the DIC pixel intensity distribution preference of basolateral sections. The APVs of the asymmetric and symmetric cells' nuclear fluorescence were 38 and 9% higher for the basolateral section than apical section of the cell. The average pixel

intensities of plasma membrane fluorescence were approximately 291 and 161% higher on the basolateral side for asymmetric and symmetric cells, respectively. Similarly, the lysosomal fluorescence intensity distributions show an 87 and 40% greater fluorescence in the basolateral side of the *z*-stack for the asymmetric and symmetric cells, respectively. Figure 4C also shows 76 and 23% increases in the basal average pixel intensities of actin fluorescence for asymmetric and symmetric cells, respectively.

Cell-shape-dependent variations in geometrical polarities were observed in the fluorescence distributions of mitochondria, endoplasmic reticulum, and tubulin (Figure 4B). Mitochondrial fluorescence distribution shows that the APVs in the basolateral section of the *z*-stack are 50% greater than the APV in the apical section of the asymmetric cells. The endoplasmic reticulum, on the other hand, shows that the cell shape causes significant alteration of fluorescence distribution patterns in the cells with asymmetric cells showing 73% more fluorescence in the basolateral section of the *z*-stack while symmetric cells show 21% more fluorescence in the apical section of the *z*-stack. Tubulin fluorescence intensity distribution shows asymmetric fluorescence distribution in the symmetric cells, which show 37% higher fluorescence intensities in the basolateral section of the *z*-stack. Figure 4F–I and Figure S6A,B show diagrammatic representations of fluorescence distribution along the *z*-, *y*-, and *x*-axes in the two cell types in the asynchronous population.

Next, we aimed to determine specific geometrical occurrences and specifically to identify the contributing octants behind the observations. For this, we plotted the normalized frequency distribution of the two subsets of cells for each organelle's fluorescence intensities for each cellular octant (Figure S7). Table 3 summarizes the octants identified to vary from the regular trend observed for the two subsets of the organellar fluorescence distribution.

**Table 3. Type of Polarity in APV Distribution in the Asymmetric and Symmetric Cells and Contributing Octants in 3D Geometric Space of Cells in an Asynchronous RAW264.7 Population**

	asymmetric cell		symmetric cell	
	polarity type	octant	polarity type	octant
whole cell	basolateral	5–8	basolateral	5–8
nucleus	basolateral	6, 8	basolateral, X-regressive	7, 8
plasma membrane	basolateral	5, 6, 8	basolateral	5–8
mitochondria	basolateral	5, 6, 8	nil	
endoplasmic reticulum	basolateral	5, 8	apical	1–4
lysosome	basolateral	7, 8	basolateral, Y-regressive	6, 7
actin	basolateral	5–8	basolateral	5–8
tubulin	nil		basolateral	5–8

**Effects of Cell Synchronization on Subcellular Component Fluorescence Distribution.** The variations in polarity were observed upon population synchronization at the G2/M phase, which was broadly categorized into three categories: (1) Preservation of polarity as is seen in DIC image analysis and induction of (2) alteration in polarity and (3) absence of polarity (Figures 3G and 5B,C). The nuclear fluorescence intensity distribution upon synchronization shows

a shift toward the apical section of the *z*-stacks in both asymmetric (75% more in the apical section) and symmetric cells (24.5% more in the apical section), as shown in Figure 5D. The alterations observed in the analysis of plasma membrane, endoplasmic reticulum, and actin show cell-shape dependency (Figure 5C). The polarity in fluorescence intensity distribution is preserved as well as altered, and this can be correlated with the two cell shapes categorized based on the cell curvature. The plasma membrane shows significant alteration in the trend with the pixel intensity favoring the apical sections by 39%. Similarly, the endoplasmic reticulum shows the basolateral section preference in symmetric cells by 8.7%. This is significantly altered from the trend observed in the symmetric cells of the asynchronous population, where we observed the apical section preference. Furthermore, the same trend can be seen in the case of actin fluorescence intensity distributions, where asymmetric cells show 102% higher basolateral preference for fluorescence accumulation (a preservation phenomenon from the asymmetric cells from the asynchronous population) while symmetric cells show 9.6% higher apical section preference for the same, which contrasts with the trend seen in the symmetric cells of the asynchronous population.

A complete absence of polarity is a cell-shape-dependent occurrence in the plasma membrane, endoplasmic reticulum, and lysosome fluorescence (where the absence of geometrical polarity is observed in the case of asymmetric cells for plasma membrane and endoplasmic reticulum and in symmetric cells in lysosomal fluorescence distribution upon synchronization, as shown in Figure 5B,C) while cell-shape independency is seen for mitochondria and tubulin where the geometrical polarities existing in the asynchronous population “disappear” on synchronization of the population cell cycle in both morphological subsets. DIC image analysis of the synchronized population reveals the preservation of the trend, with the cells still favoring the basolateral section of the *z*-stack (Figure 3G). The planar polarities earlier observed in the nuclear and lysosomal fluorescence of the symmetric cells of the asynchronous population also “disappear” upon synchronization (Figure S5). Figure 5D,E and Figure S6C–F show diagrammatic representations of fluorescence distribution along the *z*-, *y*-, and *x*-axes in the two cell types in the synchronized population. Table S7 shows the raw APV values of fluorescently labeled organelles in synchronized RAW264.7 cell population.

Furthermore, to study which of the octants contributes to the distribution polarities observed, we plotted normalized frequencies of the number of cells against APVs in each octant (Figure S8). Table 4 summarizes the octants identified to vary from the regular trend observed for the two subsets of the organellar fluorescence distribution and shape of the distribution observed.

All the observations were subjected to a two-tailed unpaired Student's *t* test using MS Excel 2016 to check the significance level of the observed differences. Tables S1, S2, and S3 mention the *p*-values of the *t* tests of different pairs. A *p*-value <0.05 was considered significant.

## DISCUSSION

The study presents a comprehensive analysis of structural pleomorphism in a naturally emergent system, a cell, while focusing on the whole (the cell) and its parts (subcellular components) (Figure 6). We have also delved into intricacies



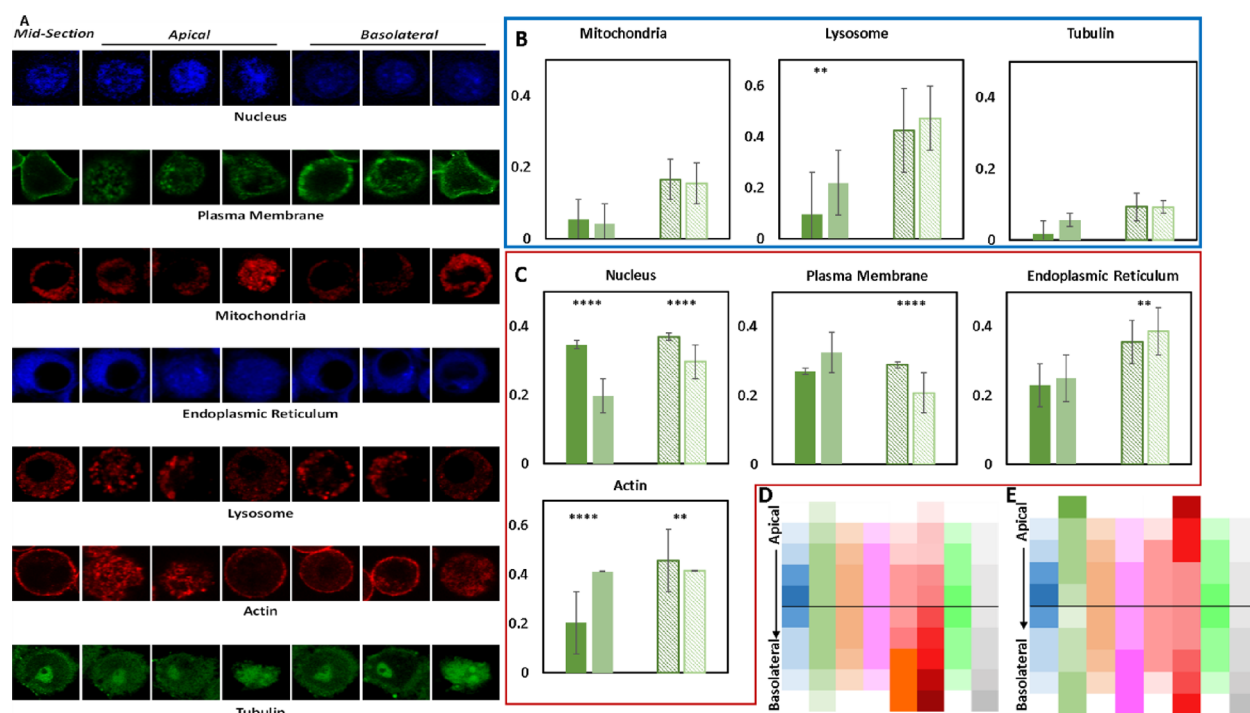


**Figure 5.** (A)  $7 \times 7$  panel of fluorescent images of different organelles in a single cell both in the synchronized RAW264.7 population. The first image of each panel is a midsection image of a single-cell organelle fluorescence from a z-stack, followed by representative images of one of the apical sections of a z-stack of three single cells, followed by their corresponding basolateral section images. (B, C) APV distribution bars in z-sections along the z-axis in the synchronized RAW264.7 cell population (mean  $\pm$  SE). Solid bars represent an asymmetric subset of cells, and patterned bars represent a symmetric cell subset. The apical sections are depicted by dark-green bars, and basolateral areas are depicted by light-green bars. The level of significance is shown by “\*”. The absence of “\*” is considered a lack of polarity. (B) (Blue) Absence of polarity in mitochondria ( $n = 153$ ), lysosome ( $n = 82$ ), and tubulin ( $n = 110$ ). (C) (Red) Induction of alteration of polarity in the nucleus ( $n = 126$ ), plasma membrane ( $n = 82$ ), endoplasmic reticulum ( $n = 153$ ), and actin ( $n = 107$ ). (D, E) are representative diagrams of the fluorescence distribution of the organelles along the z-axis, from the apical to basolateral surfaces, in asymmetric and symmetric cell subsets, respectively. The organelles, from left to right, are the nucleus (blue), plasma membrane (dull green), mitochondria (orange), endoplasmic reticulum (pink), lysosome (light red), actin (bright red), tubulin (bright green), and DIC image intensities (gray).

**Table 4. Type of Polarity in APV Distribution in the Asymmetric and Symmetric Cells and Contributing Octants in 3D Geometric Space of Cells in Synchronized RAW264.7 Population**

	asymmetric cell		symmetric cell	
	polarity type	octant	polarity type	octant
whole cell	basolateral	5–8	basolateral	5–8
nucleus	apical	1	apical	4
plasma membrane	nil		apical	4
mitochondria	nil		nil	
endoplasmic reticulum	nil		basolateral	5–8
lysosome	basolateral	6,7	nil	
actin	basolateral	6–8	apical	1,2,4
tubulin	nil		nil	

of cell population pleomorphism with the well-established heterogeneous cell shape subsets along with trying to answer how the whole-cell pixel distribution pleomorphy is being reflected in or translated into the pleomorphism of its parts. Even though there is limitation of optical resolution associated with the technique used for imaging, which does not allow accurate reflection of size and proportions of the individual subcellular organelles, the pixel information within the images still serves as a data mine to quantitatively analyze the intracellular molecular density distributions using well-established commercially available organelle-specific fluores-

cent reporters. To this aid, we have tried to examine the cells in their live hydrated state using confocal microscopy except in case of actin-labeled samples where the fixation was an essential step in the staining protocol.

We observed structural pleomorphism at both the whole-cell level and the subcellular compartmental level. The observations showed cell-shape dependency in the apico-basal direction in the case of mitochondrial, endoplasmic reticulum, and tubulin fluorescence distributions and laterally in nuclear and lysosomal fluorescence analysis. Nucleus, plasma membrane, lysosome, and actin distributions are observed to be cell-shape independent, and the whole cell’s pixel spatial pleomorphy trend of basolateral preference is being reflected in these organelles. In other words, we can say that these four organelles might be contributing toward a 3–6% pixel distribution difference between the apical and basolateral sections observed in DIC image analysis.

Having studied the morphological heterogeneity in the RAW264.7 cells at random points of time in culture, we acknowledge that the morphological changes are time-dependent and highly dynamic and vary over short intervals of time owing to different biochemical processes that occur at different levels of hierarchy within the cells and can be studied in detail using the advanced techniques that allow the real-time imaging. However, we have worked on a popular assumption that the ensemble average at a particular time point encapsulates the variations occurring within the ensemble

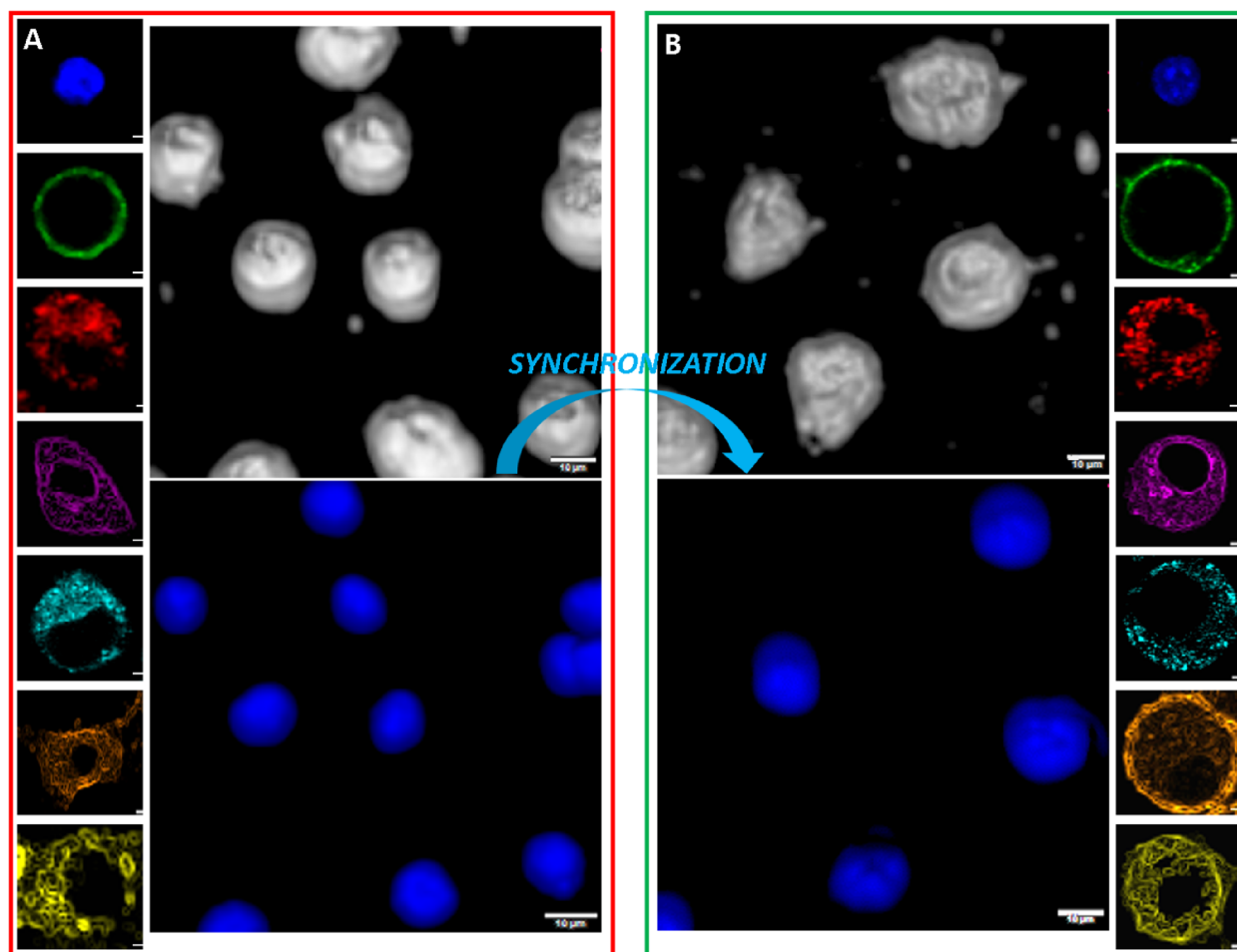


**Figure 6.** A schematic overview of the work highlighting the 3D pleomorphism at the whole-cell and subcellular component levels in the asynchronous (A) and synchronized (B) RAW264.7 population. Small 2D snippets show a single-cell representative image of the nucleus (blue), plasma membrane (green), mitochondria (red), endoplasmic reticulum (magenta), lysosome (cyan), actin (orange), and tubulin (yellow). The scale bar of the small images is 2  $\mu\text{m}$ . The whole-cell 3D projections (white) are prepared using DIC images for the corresponding nuclear projections (in blue), showing how the variation in pleomorphism at the whole-cell level is translated at the organelle level (nucleus). The scale bar of the projections is 10  $\mu\text{m}$ . It is important to note that proper interpretation of the scale bar is suggested only in images containing whole cells in 3D (i.e., white composites created from DIC images). For fluorescence images, the scale bars are for general reference only.

across different time points.<sup>16</sup> For instance, consider the scenario where a single cell is observed continuously for 10 h compared to observing 10 cells simultaneously for 1 h. The latter approach effectively integrates all potential observations that could be made on a single cell over 10 h, albeit with reduced effort. In addition, to further validate our findings, we conducted a control experiment where we synchronized the cell cycle at the G2/M phase using thymidine/nocodazole treatment that has been reported to synchronize 85% population at the G2/M phase, thus allowing maximum control over the biochemical and thereby morphological dynamics.<sup>12,15</sup> Upon synchronization, we still observed the heterogeneities (for instance, lysosomal and actin asymmetric cell polarities) previously identified in the population. This observation implies that the earlier observed morphological diversities already encompassed the variations one would expect to observe if all cells were in a single phase of the cell cycle. Thus, our results reinforce the robustness and validity of our initial observations regarding cellular and subcellular heterogeneities. Furthermore, upon synchronization at the G2/M phase, we also observe alterations in the APV distributions of nuclear, plasma membrane, lysosomal, and

actin fluorescence amounting to only a 3% decrease in the basolateral preference of the symmetric cells which in our case study validates that the whole is something else besides its parts.

The questions arise as to whether the heterogeneity observed in the component fluorescence distribution and in turn the distribution of the organelle is on the whim of the cell or has a biological relevance. Our search of RAW264.7 specific literature led us to find the functional relevance of differential placements of organelles in the three-dimensional space of the cell but not specifically in RAW264.7 cells. Macrophages have been reported to possess planar polarity with respect to nuclear placements, which further confirms our finding.<sup>17</sup> The presence of the CSEs might be one of the reasons for our observation of higher fluorescence distribution in the basolateral section of the z-sections.<sup>18</sup> Apically placed mitochondria have been reported to serve as a firewall against excess entry of  $\text{Ca}^{2+}$  ions in secretory cells.<sup>19</sup> Another study on epididymal cells suggests the apical mitochondrial population to be involved in holocrine secretion, cooperation with the principal cells in epididymal reabsorption of testicular fluid, and acidification of epididymal fluid.<sup>20</sup> A hair cell study also

reports distinct apical and basolateral mitochondrial populations.<sup>21</sup> In MDCK cells, polarized exocytosis of lysosome to the basolateral membrane occurs under the influence of calcium ionophores.<sup>22</sup> Actin has been reported to play a role in planar polarity of subcellular components like lysosomes.<sup>23,24</sup> An in-depth analysis of octant APV frequency distributions shows that actin fluorescence peaks in octants contribute to the planar polarity of nucleus and lysosome. Actin has been known to form a cortex that governs cell shape and function<sup>25,26</sup>; hence, the independent but similar changes in polarity of APV distributions of plasma membrane and actin supports our observation.

Few studies have highlighted the impact of cell-to-cell interactions between RAW264.7 cells and other cell types, leading to diverse biochemical responses such as M2 phenotype induction, polarization, differentiation, plasticity, and apoptosis, all known to influence cellular morphology.<sup>27–29</sup> Our study aimed to investigate, through image data analysis, whether intrapopulation cell-to-cell interactions influence the overall morphological symmetry of RAW264.7 cells, a morphometric parameter used to categorize the cell as either symmetric or asymmetric. This would have further indicated toward an underlying mechanism influencing the neighboring cells' morphology. While our findings suggest that whole-cell morphological symmetry remains unaffected by neighboring cell symmetry, the presence of studies implicating cell-to-cell interactions in various biochemical processes in RAW264.7 cells underscores the necessity for further exploration into the influences of cellular contacts in this context.

In Table S4, we have listed studies that have utilized optical/light microscopy data to morphometrically analyze the cells to gain a better understanding of structure and function of cells. While quite rigorous in nature, none of the studies have been able to report any subcellular components contributing/opposing the whole-cell optical densities polarities, which we have attempted to answer for the first time to our knowledge. Even so, we have barely been able to scratch the surface of a very vast field of natural emergence phenomenon and further in-depth studies using high-throughput technology are required to gain advancement in this field.

**Translational Potential of the Work.** Significant efforts have been invested in developing tools for understanding correlations between single-event and population observations, as well as extrapolating from single-cell to population characteristics (or vice versa interpolating), especially involving imaging data.<sup>30–36</sup> While there is an increasing appreciation for cellular heterogeneity in biology from evolutionary, energetic, and morphological perspectives, it is mostly phenomenology/feature/event-specific.<sup>37–47</sup> However, how the oldest form of observed heterogeneity, i.e., pleomorphism of individual cells in (populations of) cell cultures, translates to or is reflected in subcellular structures has not been systematically studied until date. This work fills that gap. Utilizing optical sectioning in confocal microscopy, this work presents a major step toward understanding the impact of overall morphological variations in cells, both at 2D and 3D levels, on subcellular components and their distribution within the cells. The image-based analyses of cell populations, while capturing details at a single-cell level, presented here can not only be translated to cell cytometry using sophisticated imaging techniques but also be applied to microtome-sectioned histological sections. The quantitative analyses developed here allow rigorous quantifi-

cation of morphological variations in subcellular components while accounting for the overall morphological heterogeneity in cells. The present study is one of the pioneering techniques that has exploited a tool usually employed to study 2D image data with a better signal:noise ratio to transition to 3D interpretations by developing an image processing algorithm that has minimized manual interventions within the limits of the technique. Further involvement of the machine learning techniques to the image processing algorithm developed in this work will allow tracking changes in ROIs around a cell leading to automation and thereby analysis with almost negligible manual interventions when similar studies are conducted using the real-time imaging techniques.<sup>48,49</sup> While research is being carried out to develop automated image-based diagnostic techniques, this would enable development of image-based diagnostics that involve separate subcellular compartments.<sup>50,51</sup> This work also lays the foundations for further development of cellular and subcellular “heterogeneity indices”. Proper analyses of “heterogeneity indices” at both the subcellular and whole-cell levels hold the promise of providing insights into cellular origins of various (clinical) pathologies, including diagnostics pertaining to compartment-specific issues. The morphological impact of potential therapeutic treatments (e.g., incubation with drug molecules) on whole cells and subcellular compartments can also be rigorously studied. In summary, the biggest translational potential of this work is the possibility of enabling rapid and rigorous “differential diagnosis” of “symptoms” at the cellular level.

## CONCLUSIONS

While the literature is rich with studies visualizing single cells and their respective organelles using many high-resolution and/or throughput imaging techniques, we, for the first time, capture the independence of three components/organelles (ER, mitochondria, and tubulin) from whole-cell pleomorphism. We also report heterogeneity in 3D distribution of nucleus, plasma membrane, lysosome, and actin in the context of pleomorphism observed at the whole-cell level—this may be interpretable as either dependency of these subcellular components on whole cells OR reflection of whole-cell morphological variations on subcellular components. Interestingly, nonbiological and artificial emergent systems lack such variations in independent or dependent relations of the “parts with the whole”.<sup>5,43</sup> As we delve deeper into the intricacies of cellular structure, our study lays the foundation for future explorations into the emergent properties of natural biological systems toward a holistic understanding of cellular life.

## ASSOCIATED CONTENT

### Supporting Information

The Supporting Information is available free of charge at <https://pubs.acs.org/doi/10.1021/acsomega.3c10062>.

Image processing flowchart; pre-image processing flowchart; pie-chart with number of neighbor distribution; significance of apv distributions in octants; lateral distributions of apvs; frequency distributions of apvs in octants; lateral projections of z-stacks; *p*-values of Student's *t*-test; and literature on optical morphometric studies (PDF)

MATLAB codes used in image processing (PDF)

## AUTHOR INFORMATION

### Corresponding Author

Aditya Mittal – Kusuma School of Biological Sciences, Indian Institute of Technology-Delhi, Delhi 110016, India;  
orcid.org/0000-0002-4030-0951; Email: amittal@bioschool.iitd.ac.in

### Author

Pragya Singh – Kusuma School of Biological Sciences, Indian Institute of Technology-Delhi, Delhi 110016, India

Complete contact information is available at:

<https://pubs.acs.org/10.1021/acsomega.3c10062>

### Author Contributions

A.M. conceived the study and assisted in experiment designing and data analyses. P.S. participated in designing experiments, carried out the experiments, collected the data, prepared the figures, and analyzed the data. P.S. and A.M. wrote the final version of the manuscript.

### Notes

The authors declare no competing financial interest.

## ACKNOWLEDGMENTS

P.S. is grateful to University Grants Commission (UGC), New Delhi, for providing fellowship support.

## ABBREVIATIONS

CSE, cell surface excesses  
DIC, differential interference contrast  
ROI, region of interest  
APV, average pixel value  
TPN, total pixel number  
DMEM, Dulbecco's modified Eagle's medium  
PBS, phosphate-buffered saline  
HBSS, Hank's Balanced Salt Solution  
FBS, fetal bovine serum  
SE, standard error  
ER, endoplasmic reticulum.

## REFERENCES

- (1) Aristotle; Ross, W. D.; Ross, D. S. *Aristotle's Metaphysics: a revised text with introduction and commentary*; Clarendon Press, 1924.
- (2) Deamer, D. Emergent phenomena in biology: the origin of cellular life. In *Planetary Systems and the Origins of Life*, Stone, J.; Higgs, P.; Pudritz, R., Eds.; Cambridge Astrobiology, Cambridge University Press: Cambridge, UK 2007; pp 89–110.
- (3) Segre, D.; Ben-Eli, D.; Deamer, D. W.; Lancet, D. The lipid world. *Orig Life Evol Biosph* **2001**, *31* (1–2), 119–145. From NLM Medline
- (4) Zhang, K. D.; Wang, G. T.; Zhao, X.; Jiang, X. K.; Li, Z. T. Vesicle self-assembly by tetrathiafulvalene derivatives in both polar and nonpolar solvents and pseudo-rotaxane mediated vesicle-to-microtube transformation. *Langmuir* **2010**, *26* (10), 6878–6882. From NLM
- (5) Singh, H.; Pragya, P.; Mittal, A.; Haridas, V. Pseudopeptosomes: non-lipidated vesicular assemblies from bispidine-appended pseudopeptides. *Org. Biomol Chem.* **2023**, *21* (17), 3557–3566. From NLM Medline
- (6) Park, C.; Lim, J.; Yun, M.; Kim, C. Photoinduced release of guest molecules by supramolecular transformation of self-assembled aggregates derived from dendrons. *Angew. Chem., Int. Ed. Engl.* **2008**, *47* (16), 2959–2963. From NLM Medline
- (7) Hutchison, C. A., 3rd; Chuang, R. Y.; Noskov, V. N.; Assad-Garcia, N.; Deerinck, T. J.; Ellisman, M. H.; Gill, J.; Kannan, K.; Karas, B. J.; Ma, L.; et al. Design and synthesis of a minimal bacterial genome. *Science* **2016**, *351* (6280), aad6253. From NLM Medline
- (8) Altschuler, S. J.; Wu, L. F. Cellular heterogeneity: do differences make a difference? *Cell* **2010**, *141* (4), 559–563. From NLM Medline
- (9) Mattiazzi Usaj, M.; Yeung, C. H. L.; Friesen, H.; Boone, C.; Andrews, B. J. Single-cell image analysis to explore cell-to-cell heterogeneity in isogenic populations. *Cell Syst* **2021**, *12* (6), 608–621. From NLM Medline
- (10) Heinrich, L.; Bennett, D.; Ackerman, D.; Park, W.; Bogovic, J.; Eckstein, N.; Petruncio, A.; Clements, J.; Pang, S.; Xu, C. S.; et al. Whole-cell organelle segmentation in volume electron microscopy. *Nature* **2021**, *599* (7883), 141–146. From NLM Medline
- (11) Xu, C. S.; Pang, S.; Shtengel, G.; Muller, A.; Ritter, A. T.; Hoffman, H. K.; Takemura, S. Y.; Lu, Z.; Pasolli, H. A.; Iyer, N.; et al. An open-access volume electron microscopy atlas of whole cells and tissues. *Nature* **2021**, *599* (7883), 147–151. From NLM Medline
- (12) Apraiz, A.; Mitxelena, J.; Zubiaga, A. Studying Cell Cycle-regulated Gene Expression by Two Complementary Cell Synchronization Protocols. *J. Vis Exp* **2017**, *124*, No. e55745, DOI: 10.3791/55745. From NLM Medline
- (13) Yayon, N.; Dudai, A.; Vrieler, N.; Amsalem, O.; London, M.; Soreq, H. Intensify3D: Normalizing signal intensity in large heterogenic image stacks. *Sci. Rep* **2018**, *8* (1), 4311. From NLM Medline
- (14) Kojima, T.; Saito, K.; Kakai, T.; Obata, Y.; Saigusa, T. Circularity ratio. A certain quantitative expression for the circularity of a round figure. *Okajimas Folia Anat Jpn.* **1971**, *48* (2), 153–161. From NLM Medline.
- (15) Sanger, J. W.; Sanger, J. M. Surface and shape changes during cell division. *Cell Tissue Res.* **1980**, *209* (2), 177–186. From NLM Medline
- (16) Laporte, M. H.; Gambarotto, D.; Bertiaux, E.; Bournonville, L.; Louvel, V.; Nunes, J. M.; Borgers, S.; Hamel, V.; Guichard, P. Time-series reconstruction of the molecular architecture of human centriole assembly. *Cell* **2024**. DOI: 1872158. From NLM Publisher
- (17) Gundersen, G. G.; Worman, H. J. Nuclear positioning. *Cell* **2013**, *152* (6), 1376–1389. From NLM Medline
- (18) Kapustina, M.; Li, D.; Zhu, J.; Wall, B.; Weinreb, V.; Cheney, R. E. Changes in cell surface excess are coordinated with protrusion dynamics during 3D motility. *Biophys. J.* **2023**, *122* (18), 3656–3677. From NLM Medline
- (19) Parekh, A. B. Mitochondrial regulation of intracellular Ca<sup>2+</sup> signaling: more than just simple Ca<sup>2+</sup> buffers. *News Physiol Sci.* **2003**, *18*, 252–256. From NLM
- (20) Martinez-Garcia, F.; Regadera, J.; Cobo, P.; Palacios, J.; Paniagua, R.; Nistal, M. The apical mitochondria-rich cells of the mammalian epididymis. *Andrologia* **1995**, *27* (4), 195–206. From NLM Medline
- (21) O'Sullivan, J. D. B.; Bullen, A.; Mann, Z. F. Mitochondrial form and function in hair cells. *Hear Res.* **2023**, *428*, No. 108660. From NLM Medline
- (22) Xu, J.; Toops, K. A.; Diaz, F.; Carvajal-Gonzalez, J. M.; Gravotta, D.; Mazzoni, F.; Schreiner, R.; Rodriguez-Boulan, E.; Lakkaraju, A. Mechanism of polarized lysosome exocytosis in epithelial cells. *J. Cell Sci.* **2012**, *125* (24), 5937–5943. From NLM Medline
- (23) Cordonnier, M. N.; Dauzonne, D.; Louvard, D.; Coudrier, E. Actin filaments and myosin I alpha cooperate with microtubules for the movement of lysosomes. *Mol. Biol. Cell* **2001**, *12* (12), 4013–4029. From NLM Medline
- (24) Kim, D. H.; Wirtz, D. Cytoskeletal tension induces the polarized architecture of the nucleus. *Biomaterials* **2015**, *48*, 161–172. From NLM Medline
- (25) Chalut, K. J.; Paluch, E. K. The Actin Cortex: A Bridge between Cell Shape and Function. *Developmental Cell* **2016**, *38* (6), 571–573.
- (26) Chugh, P.; Clark, A. G.; Smith, M. B.; Cassani, D. A. D.; Dierkes, K.; Ragab, A.; Roux, P. P.; Charras, G.; Salbreux, G.; Paluch,

- E. K. Actin cortex architecture regulates cell surface tension. *Nat. Cell Biol.* **2017**, *19* (6), 689–697. From NLM Medline
- (27) Kong, L.; Smith, W.; Hao, D. Overview of RAW264.7 for osteoclastogenesis study: Phenotype and stimuli. *J. Cell Mol. Med.* **2019**, *23* (5), 3077–3087. From NLM Medline
- (28) Konishi, H.; Haga, Y.; Okumura, M.; Tsujino, H.; Higashisaka, K.; Tsutsumi, Y. Coculture with macrophages alters ferroptosis susceptibility of triple-negative cancer cells. *Cell Death Discov* **2024**, *10* (1), 108. From NLM PubMed-not-MEDLINE
- (29) Ibi, M.; Horie, S.; Kyakumoto, S.; Chosa, N.; Yoshida, M.; Kamo, M.; Ohtsuka, M.; Ishisaki, A. Cell–cell interactions between monocytes/macrophages and synoviocyte-like cells promote inflammatory cell infiltration mediated by augmentation of MCP-1 production in temporomandibular joint. *Biosci. Rep.* **2018**, *38*, BSR20171217. Artn Bsr20171217 10.1042/Bsr20171217
- (30) Mittal, A.; Leikina, E.; Bentz, J.; Chernomordik, L. V. Kinetics of influenza hemagglutinin-mediated membrane fusion as a function of technique. *Anal. Biochem.* **2002**, *303* (2), 145–152.
- (31) Mittal, A.; Shanguan, T.; Bentz, J. Measuring pKa of activation and pKi of inactivation for influenza hemagglutinin from kinetics of membrane fusion of virions and of HA expressing cells. *Biophys. J.* **2002**, *83* (5), 2652–2666. From NLM Medline
- (32) Mittal, A.; Leikina, E.; Chernomordik, L. V.; Bentz, J. Kinetically differentiating influenza hemagglutinin fusion and hemifusion machines. *Biophys. J.* **2003**, *85* (3), 1713–1724. From NLM Medline
- (33) Arora, S.; Bhat, V.; Mittal, A. Correlating single cell motility with population growth dynamics for flagellated bacteria. *Biotechnol. Bioeng.* **2007**, *97* (6), 1644–1649. From NLM Medline
- (34) Gupta, R.; Mishra, P.; Mittal, A. Enhancing nucleic acid detection sensitivity of propidium iodide by a three nanometer interaction inside cells and in solutions. *J. Nanosci Nanotechnol* **2009**, *9* (4), 2607–2615. From NLM Medline
- (35) Naresh, M.; Gopinadhan, K.; Sekhar, S. H.; Juneja, P.; Sharma, M.; Mittal, A. NSOM/HRTEM Characterization of Biologically Derived Cubo–Octahedral Nanomagnets. *IEEE Trans. Magn.* **2009**, *45*, 4861–4864.
- (36) Singh, S.; Ponnappan, N.; Verma, A.; Mittal, A. Osmotic tolerance of avian erythrocytes to complete hemolysis in solute free water. *Sci. Rep* **2019**, *9* (1), 7976. From NLM Medline
- (37) Sharma, M.; Naresh, M.; Mittal, A. Morphological changes in magnetotactic bacteria in presence of magnetic fields. *J. Biomed Nanotechnol* **2007**, *3* (1), 75–80.
- (38) Gattegno, T.; Mittal, A.; Valansi, C.; Nguyen, K. C. Q.; Hall, D. H.; Chernomordik, L. V.; Podbilewicz, B. Genetic control of fusion pore expansion in the epidermis of. *Mol. Biol. Cell* **2007**, *18* (4), 1153–1166.
- (39) Naresh, M.; Hasija, V.; Sharma, M.; Mittal, A. Synthesis of Cellular Organelles Containing Nano-Magnets Stunts Growth of Magnetotactic Bacteria. *J. Nanosci Nanotechnol* **2010**, *10* (7), 4135–4144.
- (40) Naresh, M.; Sharma, M.; Mittal, A. Intracellular Magneto-Spatial Organization of Magnetic Organelles Inside Intact Bacterial Cells. *J. Biomed Nanotechnol* **2011**, *7* (4), 572–577.
- (41) Naresh, M.; Das, S.; Mishra, P.; Mittal, A. The chemical formula of a magnetotactic bacterium. *Biotechnol. Bioeng.* **2012**, *109* (5), 1205–1216.
- (42) Singh, S.; Mittal, A. Transmembrane Domain Lengths Serve as Signatures of Organismal Complexity and Viral Transport Mechanisms. *Sci. Rep.* **2016**, *6*, 22352. DOI: ARTN 2235210.1038/srep22352
- (43) Mittal, A.; Singh, S. Insights into eukaryotic evolution from transmembrane domain lengths. *J. Biomol Struct Dyn* **2018**, *36* (8), 2194–2200.
- (44) Agrawal, A.; Scott, Z. C.; Koslover, E. F. Morphology and Transport in Eukaryotic Cells. *Annual Review of Biophysics* **2022**, *51*, 247–266.
- (45) Firdos; Mittal, A. Secretory Conservation in Insulin Producing Cells: Is There a System-Level Law of Mass Action in Biology? *ACS Omega* **2023**, *8* (40), 37573–37583.
- (46) Firdos; Pramanik, T.; Verma, P.; Mittal, A. (Re-)Viewing Role of Intracellular Glucose Beyond Extracellular Regulation of Glucose-Stimulated Insulin Secretion by Pancreatic Cells. *ACS Omega* **2024**, *9* (10), 11755–11768. From NLM PubMed-not-MEDLINE
- (47) Mittal, A.; Grover, R. Self-Assembly of Biological Membranes into 200–400 nm Aqueous Compartments. *J. Nanosci Nanotechnol* **2010**, *10* (5), 3085–3090.
- (48) Garrett, N.; Whiteman, M.; Moger, J. Imaging the uptake of gold nanoshells in live cells using plasmon resonance enhanced four wave mixing microscopy. *Opt Express* **2011**, *19* (18), 17563–17574. From NLM Medline
- (49) Pal, R.; Basu Thakur, P.; Li, S.; Minard, C.; Rodney, G. G. Real-time imaging of NADPH oxidase activity in living cells using a novel fluorescent protein reporter. *PLoS One* **2013**, *8* (5), No. e63989. From NLM Medline
- (50) Foran, D. J.; Chen, W.; Yang, L. Automated image interpretation and computer-assisted diagnostics. *Stud. Health. Technol. Inform.* **2013**, *185*, 77–108. From NLM Medline
- (51) Yan, J.; Lai, Y.; Xu, Y.; Zheng, Y.; Niu, Z.; Tan, T. Editorial: Artificial intelligence-based medical image automatic diagnosis and prognosis prediction. *Front. Phys.* **2023**, *11*, No. 1210010.